Chapter 6

Numerical Simulation and Results

The performance of the algorithm is studied in a series of test cases. The first set of examples is designed to verify analytical results. A second set of test cases illustrates the performance of the method for heterogeneous media. Finally, a real world problem is presented.

6.1 Computer code

To implement the algorithm the simulator Parssim 1 was modified. This code was developed by the Center for Subsurface Modeling (CSM) of the Texas Institute for Computational and Applied Mathematics (TICAM) at the University of Texas at Austin [1]. Parssim1 models aquifer or reservoir incompressible single phase fluid flow and reactive transport through a heterogeneous porous medium. Dependence of the porosity on time was implemented along with porosity-dependent permeability. An outer flow-transport loop on each time step was also added to account
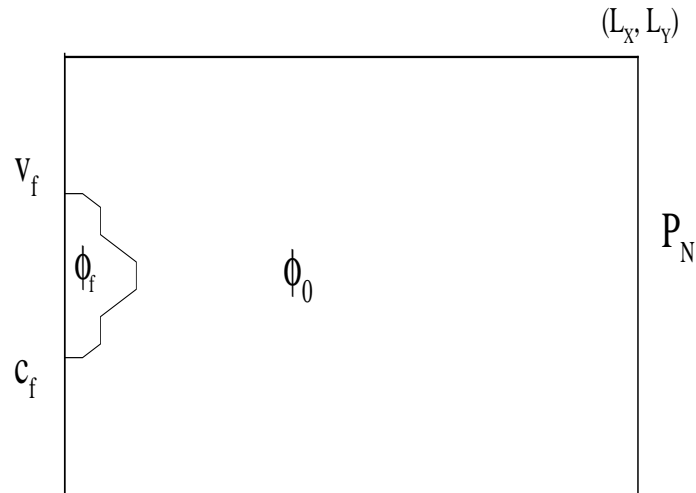
(L_X, L_Y)

v_f

ϕ_f ϕ_0

P_N

c_f

Figure 6.1: Numerical Domain

for the tight and highly nonlinear coupling. Other modifications and additions to the code were made to accommodate the given problem.

6.2 Domain

The numerical simulation of reaction infiltration instabilities is carried out in a rectangular domain as shown in Figure 6.1 . The system is solved using the boundary and initial conditions (3.7), (3.8), and (3.9). At the left side both the inlet flow velocity v_f and concentration c_f are specified. No-flow conditions are imposed at the top and bottom boundaries, while a pressure value p_N is specified at the right (outflow) side. The simulation is started with an initial bump in porosity and concentration. Behind

Δt	$\|\phi_h - \phi\|_2$	$\|C_h - c\|_2$
1	2.0785E-05	1.2362E-05
.5	0	5.7094E-06
.25	0	2.4771E-06
.125	0	8.7063E-07

Table 6.1: Rate of convergence with $V_f = 10$ cm/day

the bump the porosity and concentration are at their final values ϕ_f and c_f, while elsewhere they are at equilibrium values ϕ_o and c_{eq}, respectively.

6.3   Rate of convergence

Since the exact solution of the problem is not known, to test the convergence of the algorithm numerically we run the algorithm for different Δt and take the result of the smallest Δt as the best approximation to the exact solution. The 2-norm of the difference between this solution and the rest is computed and the results are given in Tables 6.1 and 6.2 for different inlet velocity.

6.4   Verification of the analytical results

In this section we list some of the analytical results obtained in the previous analysis of the problem in order to verify them numerically.

Δt	$\|\phi_h - \phi\|_2$	$\|C_h - c\|_2$
1	7.7942E-04	8.8489E-05
.5	4.3648E-04	4.0246E-05
.25	3.1177E-04	1.7093E-05
.125	7.2746E-05	5.6064E-06

Table 6.2: Rate of convergence with $V_f = 100$ cm/day

6.4.1 Front velocity

The velocity of a planar, traveling wave solution can be computed from (2.2) and (2.4). Following the same techniques used in [12], we introduce a coordinate system (ζ, t) moving with the front, $\zeta = x - Vt$, where V is the front velocity. Then the equations for a planar front can be written as:

$$u' = V\phi'$$

$$-V(c\phi)' + (cu - Dc')' = -\rho V\phi'$$

Integrating from 0 to R and using the boundary conditions:

$$c \to 0, \ \phi \to \phi_f, \ u = v_f \text{ as } x \to \infty$$

$$c \to c_{eq}, \ \phi \to \phi_0, \ u = v_0 \text{ as } x \to -\infty$$

we get

$$v_0 - v_f = V(\phi_0 - \phi_f) \tag{6.1}$$

$$V(c_{eq}\phi_0 + \rho(\phi_f - \phi_0)) = c_{eq}v_0 \tag{6.2}$$

then we can solve these equations for v_0 and V and get:

$$v_0 = \frac{\epsilon\phi_0 + \phi_f - \phi_0}{\epsilon\phi_f + \phi_f - \phi_0} v_f \tag{6.3}$$

$$V = \frac{\epsilon}{\phi_f(1 + \epsilon - \frac{\phi_0}{\phi_f})} v_f \tag{6.4}$$

where $\epsilon = c_{eq}/\rho$. Since in general the solid molar density ρ greatly exceeds the solute concentration, ϵ is a small parameter which implies that the reaction zone advances with a slower speed than the fluid flow. The velocity of the front is approximated from the graph of the numerical test output and we also get the values of the velocity ahead of the front from the output data files. The comparison with the analytical value is listed in Table 6.3, where the following values are used for the other parameter $\phi_0 = .25, \phi_f = .3, c = .01, \rho = 1$ which give the following analytical ratio:

$$\frac{V}{v_f} = 0.18867925,$$

$$\frac{v_0}{v_f} = 0.99056604.$$

v_f	V	$\frac{V}{v_f}$	v_0	$\frac{v_0}{v_f}$
100	12.5	0.125	99.324	0.99324
80	9.375	0.1172	79.00	0.993028
70	8.6	0.1228	69.55	0.99357
50	6.25	0.125	49.655	0.993096
35	4.3	0.1228	34.7199	0.99199714

Table 6.3: front velocity

6.4.2 Reaction zone thickness

The thickness of the reaction zone can also be estimated [13] to be

$$L_r = \frac{V}{kc_{eq}}.$$

With the typical values of the parameters $v_f, \phi_0, \phi_f, c_{eq}$, and k the reaction zone is quite narrow. For example, with the values used in the numerical simulation $L_r \approx 10$ cm while the length of the domain is greater than 10^4 cm. Thus in order to verify this a very fine mesh has to be used which will make the computation too costly. Therefore, using only the graphs of the output, we verify this by seeing that the thickness is between 1 to 3 cells of the used mesh.

6.5 Test cases

In previous work [12] it was shown that when the Peclet number exceeds a critical number the reaction zone loses stability. Peclet number is defined to be

$$Pe = \frac{v_f L}{D},$$

where D is the diffusion coefficient and L is the width of the channel ($L = L_Y$). Both L and D are fixed in the numerical tests while v_f is used as the control parameter. In all of the test cases the value of the reaction rate constant, k, is set to 1, unless a different value is mentioned.

In the following three examples we show the three different shapes the reaction zone can attain. The values of v_f in the three cases are $10, 100, and 1$ cm/day respectively. In the examples shown in Figures 6.2 and 6.3 the following values are used:

$$\phi_0 = .25, \phi_f = .3, c_{eq} = .01, D = 10cm^2/day$$

while in the example shown in Figure 6.4 the values of the initial porosity is changed to $\phi_0 = .28$ in order to increase the nonlinearity and ensure that fingering occurs within the specified domain. A stable case is shown in Figure 6.2. A case where the reaction zone returns to a planar shape is shown in Figure 6.3. An unstable case is shown in Figure 6.4. Note that in this case, as mentioned in Chapter 1, the flow is focused at the tip of the bump as it can be seen in the velocity vector plot of Figure 6.4.

concentration   porosity

velocity field (arrows) and x-velocity (shade)
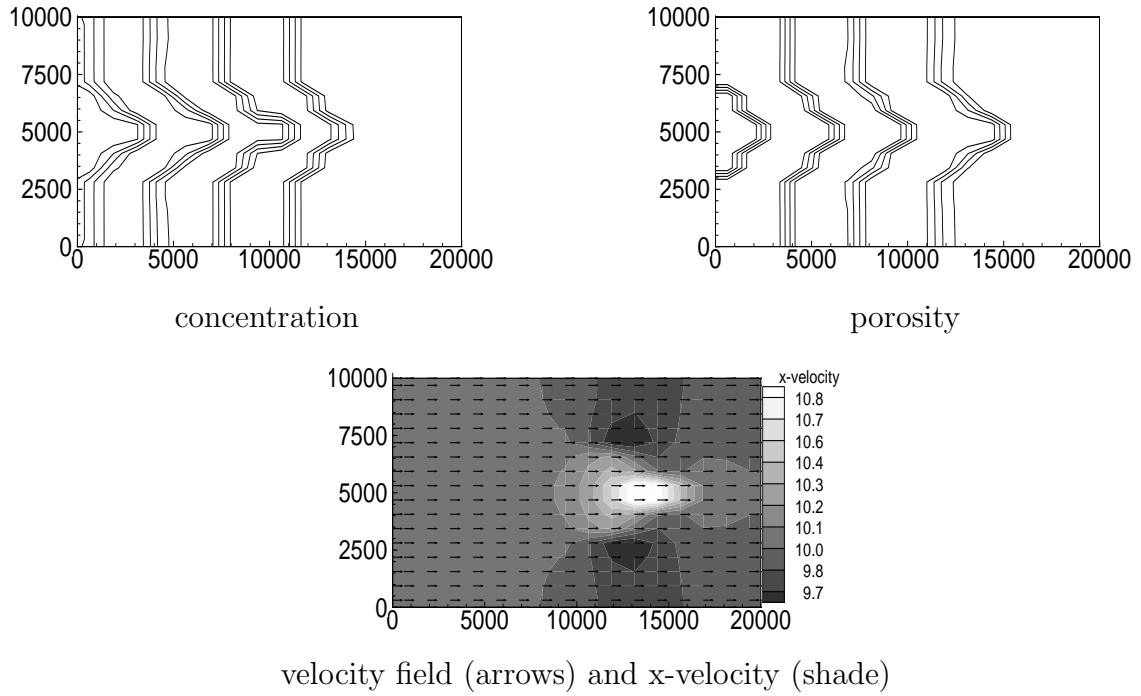
Figure 6.2: Solution contours in the stable case; $v_f = 10$ cm/day

concentration   porosity

velocity field (arrows) and x-velocity (shade)
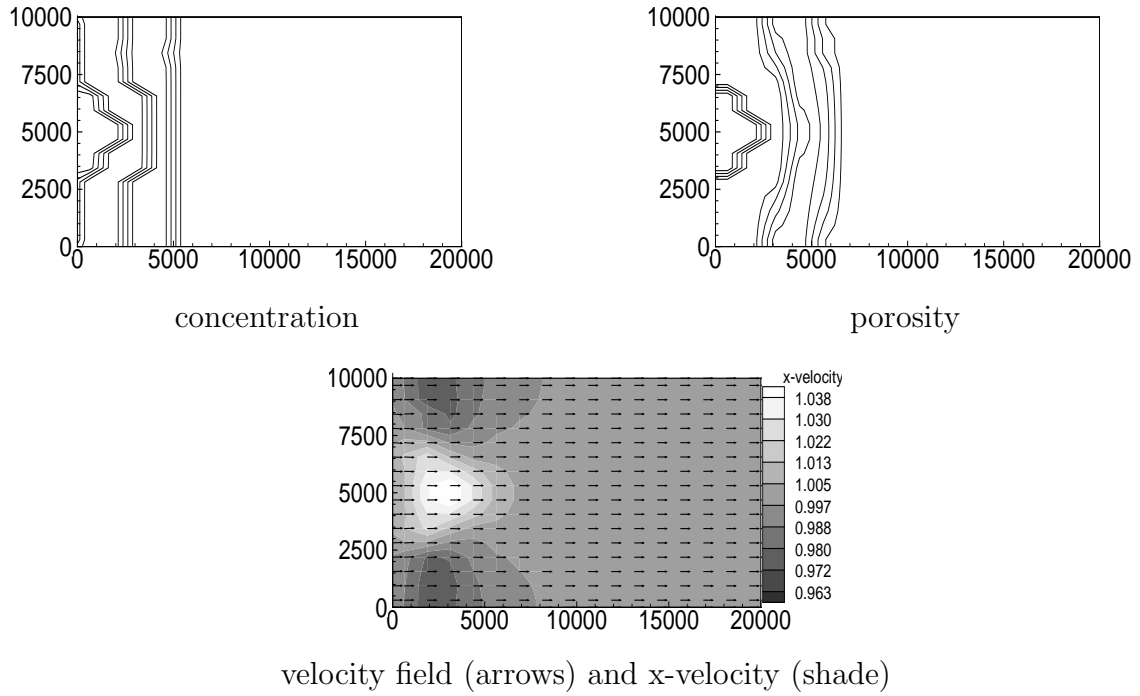
Figure 6.3: Solution contours in the planar case; $v_f = 1$ cm/day

concentration

porosity

velocity field (arrows) and x-velocity (shade)
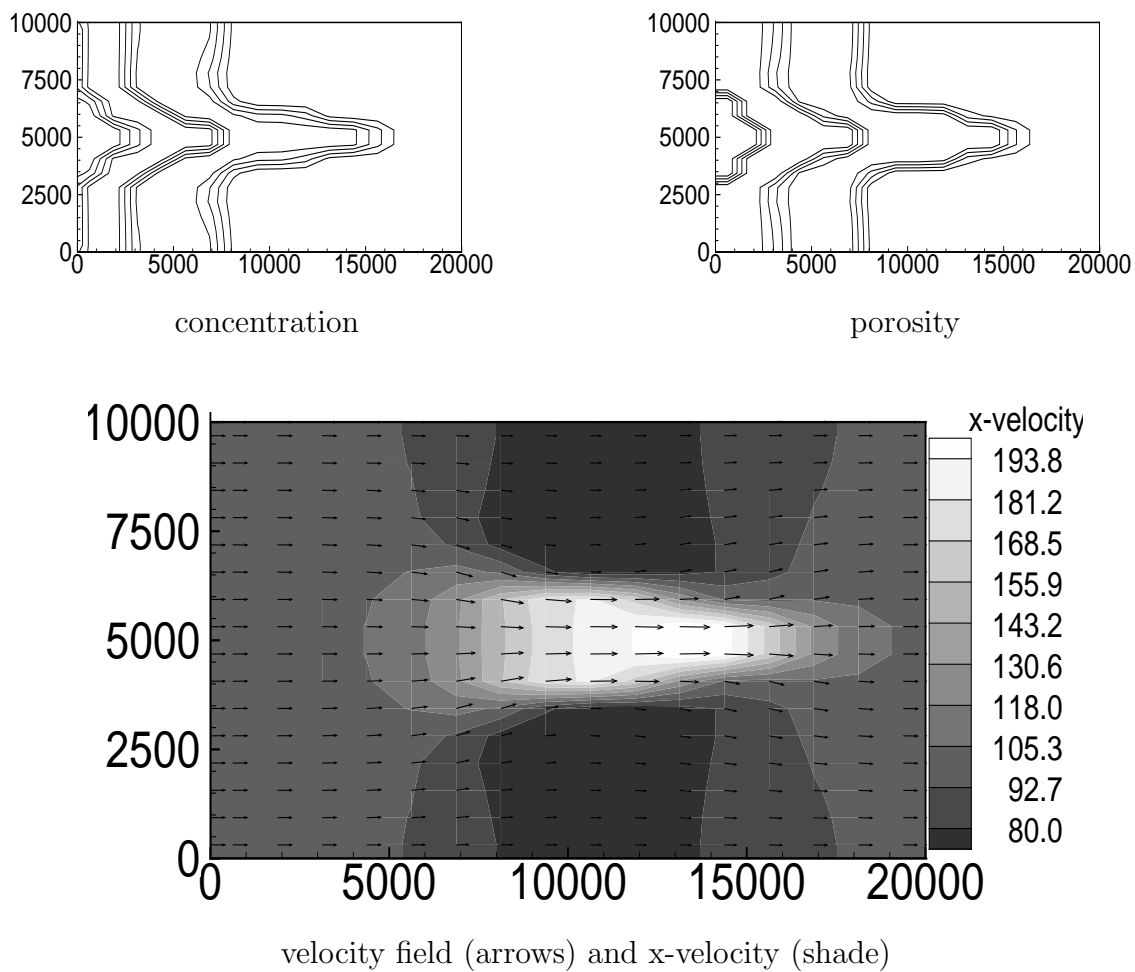
Figure 6.4: Solution contours in the unstable case; $v_f = 100$ cm/day

6.6 Dispersion effect

Since Peclet number depends on molecular diffusion, it is not clear from the analysis in [12] if hydrodynamic dispersion will affect the shape stability of the reactive flow. Therefore, in [13] the effect of hydrodynamic dispersion was examined. It was showen there that even if velocity-dependent dispersion is included in the model, the Reaction-Infiltration Instability persists. The transverse dispersion has a stabilizing effect without entirely eliminating the Reaction-Infiltration Instability [13]. We show this numerically in Figures 6.5 and 6.6. We notice that when a_T is set to $100cm$ the instability is reduced.
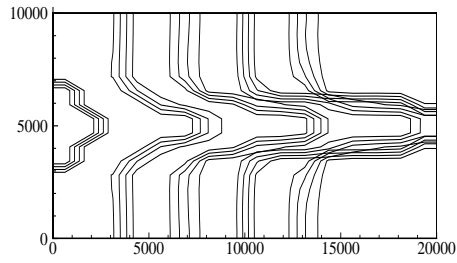
$a_L = a_T = 0$ cm
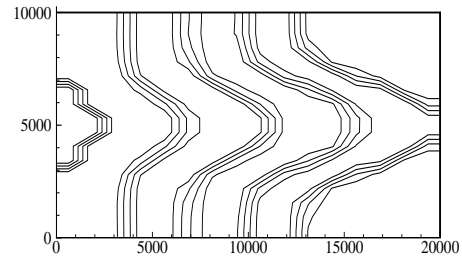
$a_L = 0$ cm, $a_T = 100$ cm
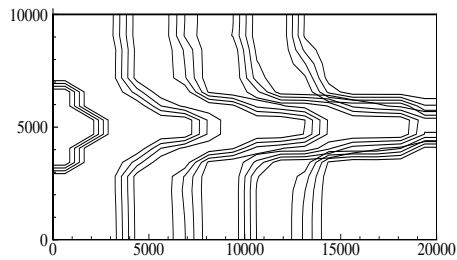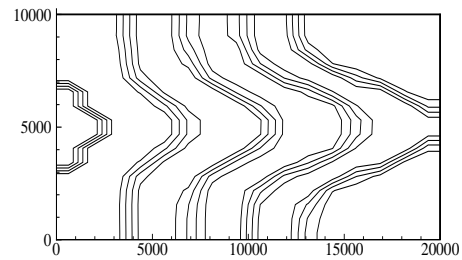
$a_L = 100$ cm, $a_T = 0$ cm

$a_L = 100$ cm, $a_T = 100$ cm

Figure 6.5: Solution contours for the porosity with $v_f = 100 cm/day$ and $D = 10 cm^2/day$

52

$a_L = a_T = 0$ cm

$a_L = 0$ cm, $a_T = 100$ cm

$a_L = 100$ cm, $a_T = 0$ cm

$a_L = 100$ cm, $a_T = 100$ cm
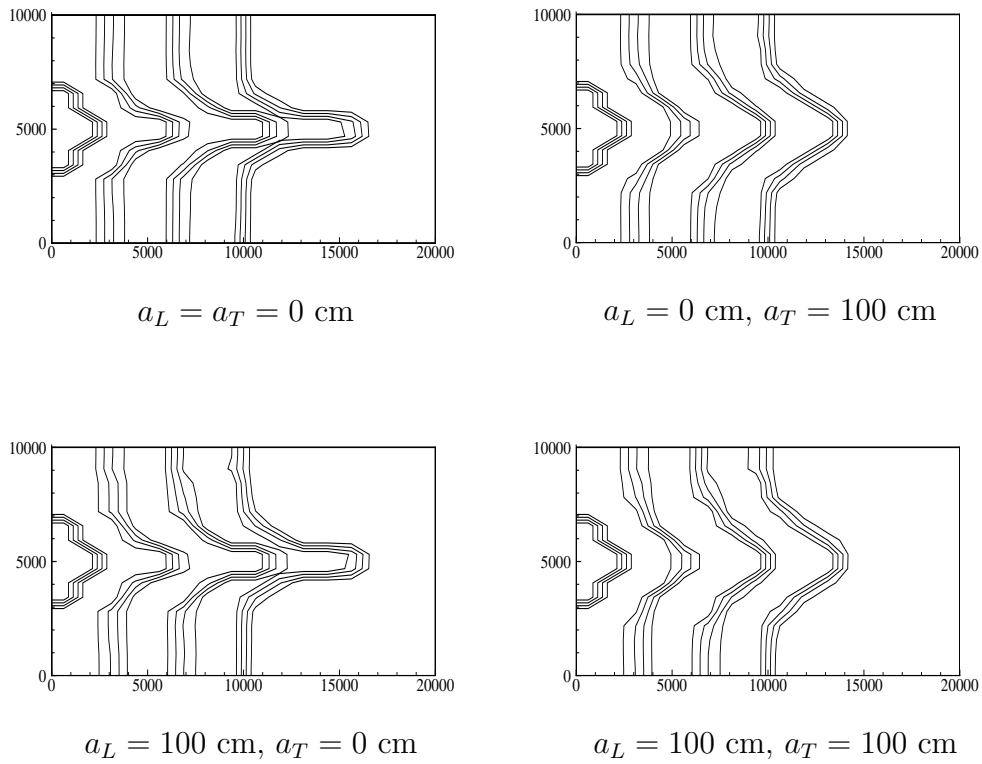
Figure 6.6: Solution contours for the porosity with $v_f = 10cm/day$ and $D = 10cm^2/day$

6.7   Non homogeneous porous media

We will consider two types of non homogeneous media, a layered porous media and a random heterogeneous porous media

6.7.1   Layered porous media

Understanding the shape stability of a reactive front in a layered porous medium is very important from the viewpoint of application because many porous media were naturally formed in a layered pattern. Using a complete linearized stability analysis, the shape stability of the reaction interface for reactive flow in a layered porous medium was studied in [16]. In that study, the layering of the porous medium is assumed to be the same as the thickness of the front and they compared the results with the case of homogeneous porous media.

As in [16] we will consider the two cases: layering only ahead of the front and layering ahead and behind the front. In the first case the porosity is constant behind the front, while in the second case a similar layered medium is left behind the front with higher porosity. For both cases as the front passes a fixed proportion of the medium dissolved out.

For the first case, layering only ahead of the front, we will use a number of layers with ϕ_0 alternating between 0.25 and 0.2 and set $\phi_f = 0.3$. For the second case, layering ahead and behind the front, ϕ_f will be set to be 0.3 and 0.24 respectively
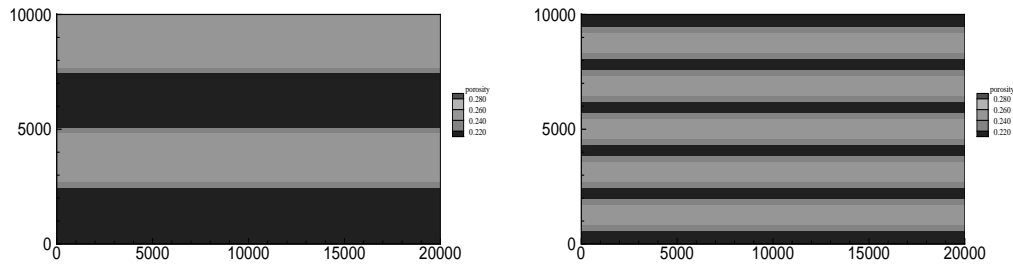
Figure 6.7: Layered porous medium

for the same pattern. To see the effect of the number of layers (or equivalently the thickness of the layers), we run both cases into two different layered medium shown in Figure 6.7. No initial bump is used in these simulations and we make no assumption about the thickness of the layers.

The results for the first case are shown in Figures 6.8–6.15. We first note that in the case with fewer layers the fingers developed are slightly longer than the ones with more layering.
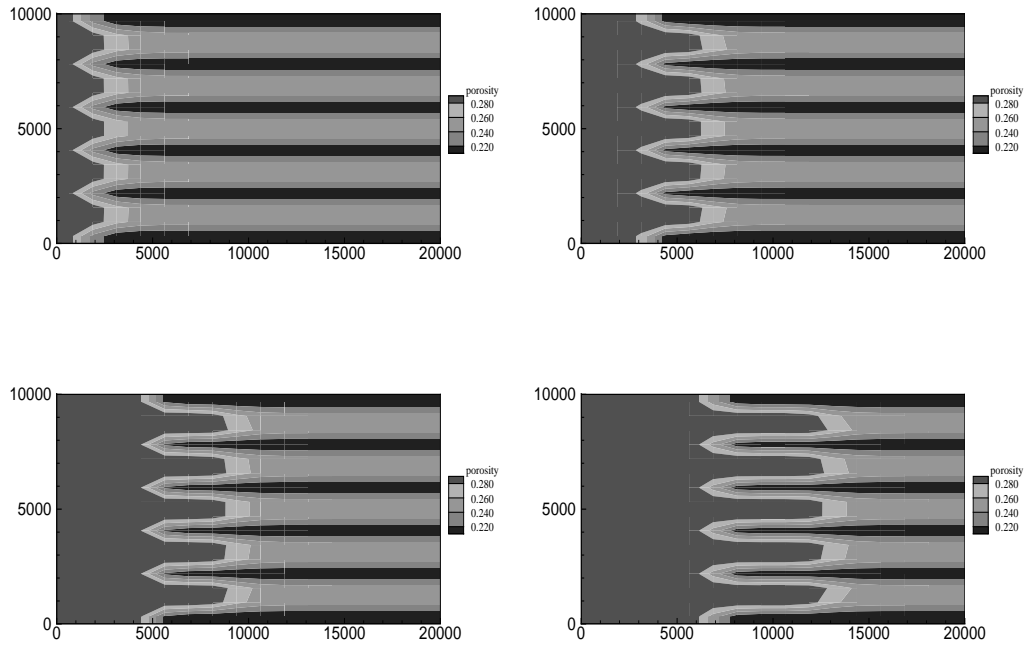
Figure 6.8: Solution contours for the porosity in Layered Porous Media ahead of the front with $V_f = 100$ cm/day
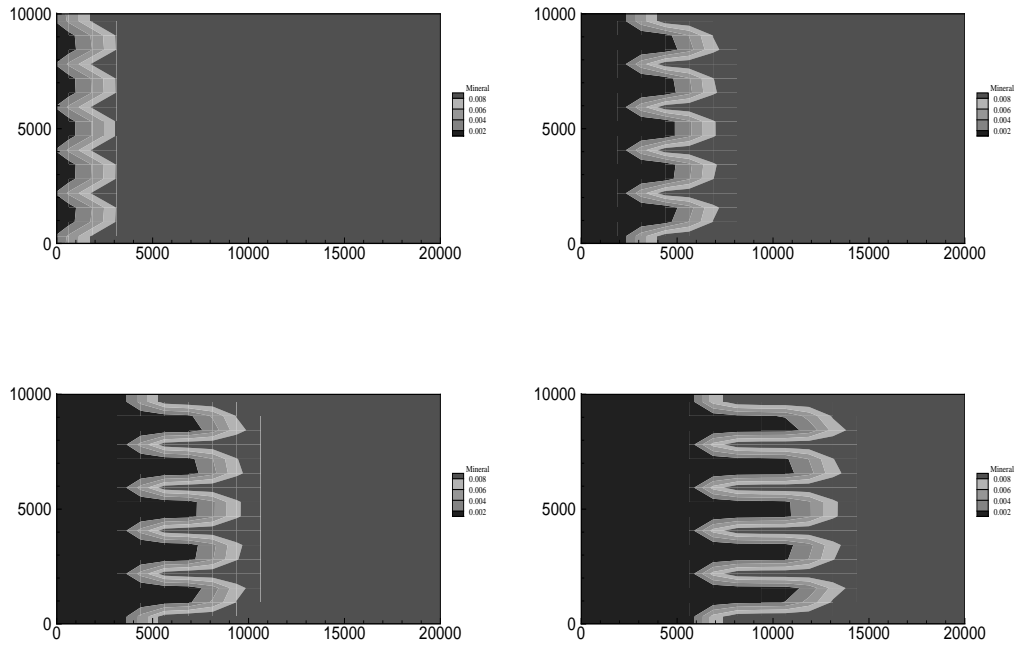
Figure 6.9: Solution contours for the concentration in Layered Porous Media ahead of the front with $V_f = 100$ cm/day
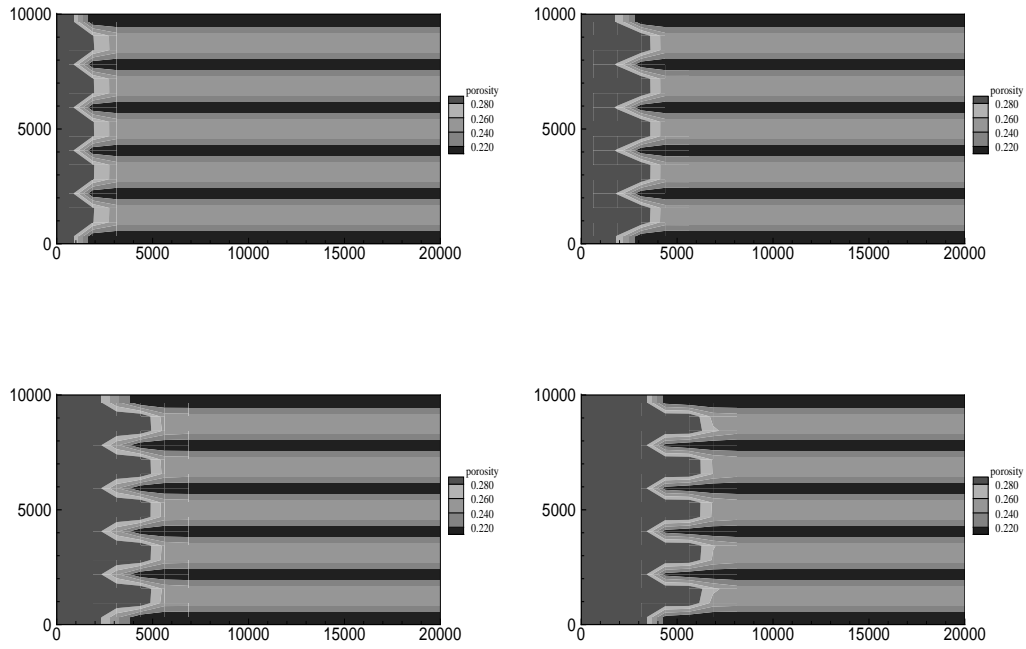
Figure 6.10: Solution contours for the porosity in Layered Porous Media with $V_f = 10$ cm/day
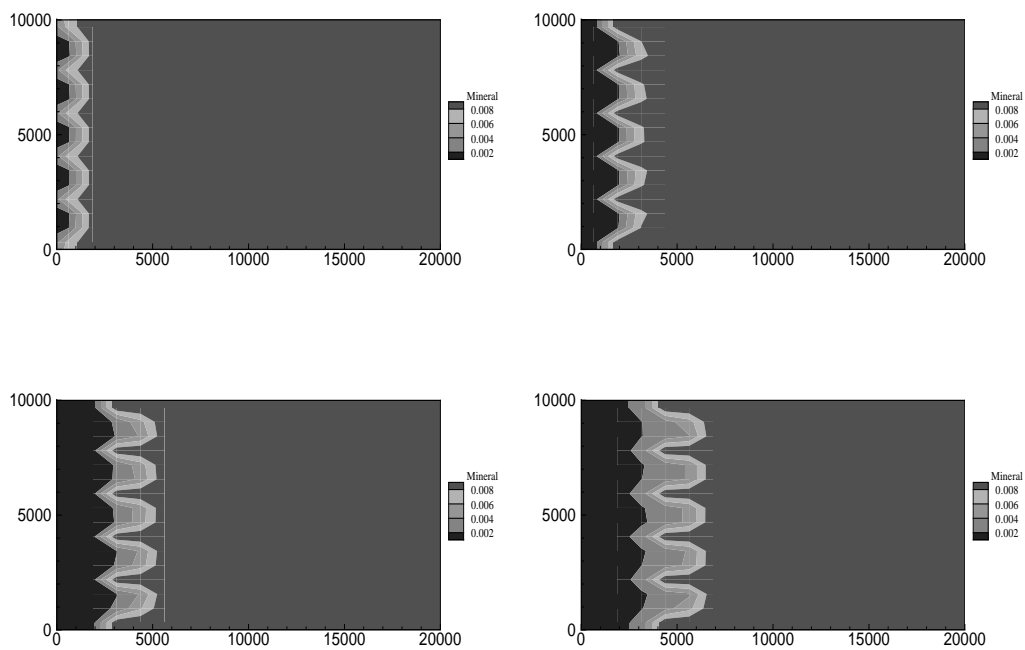
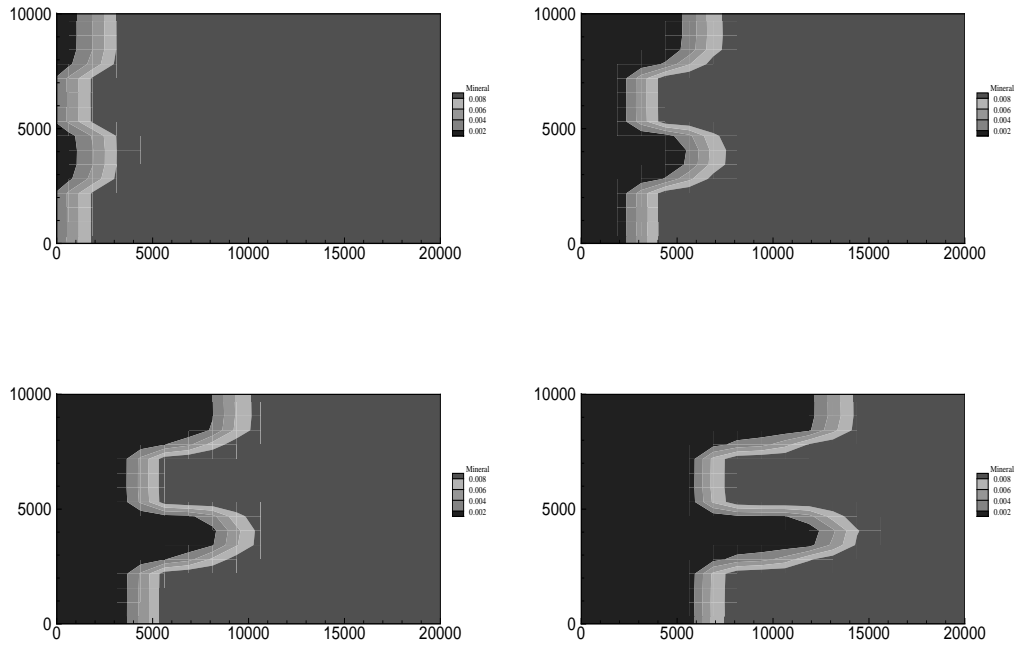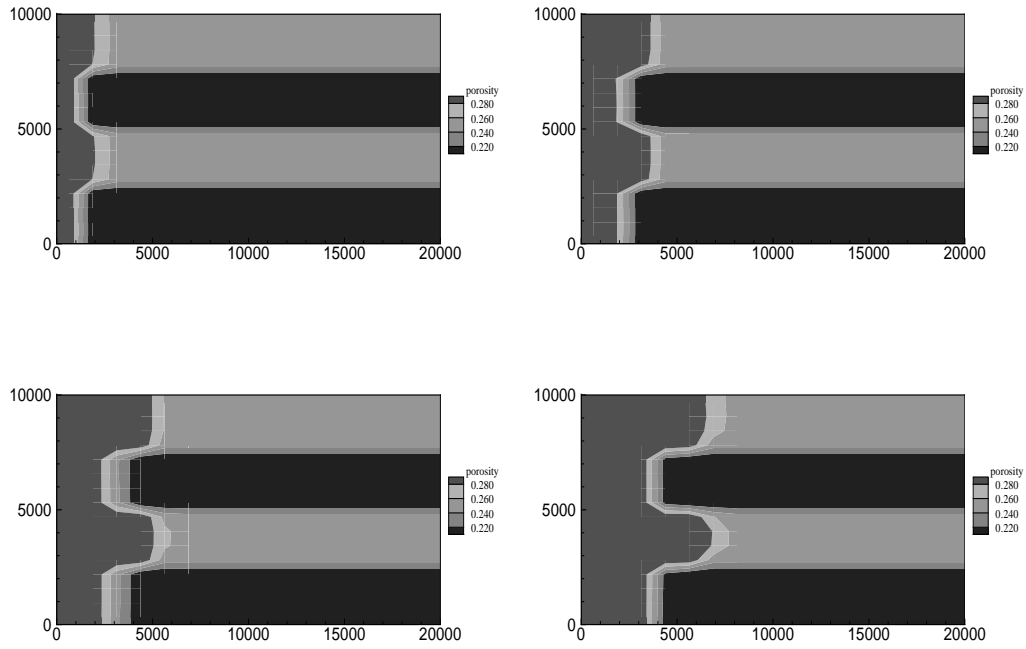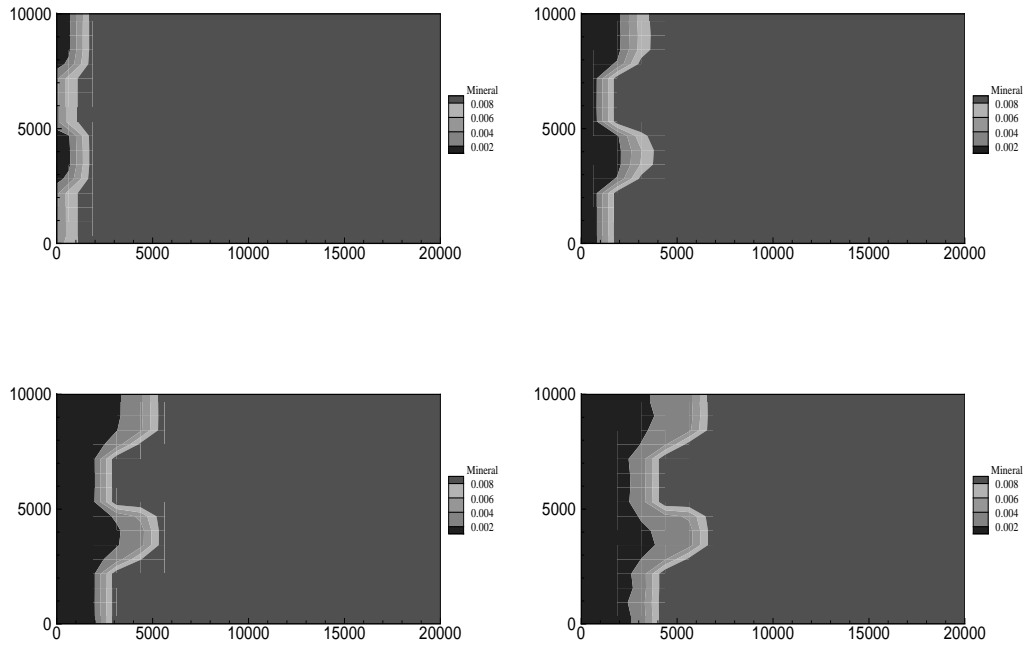Figure 6.11: Solution contours for the concentration in Layered Porous Media with $V_f = 10$ cm/day
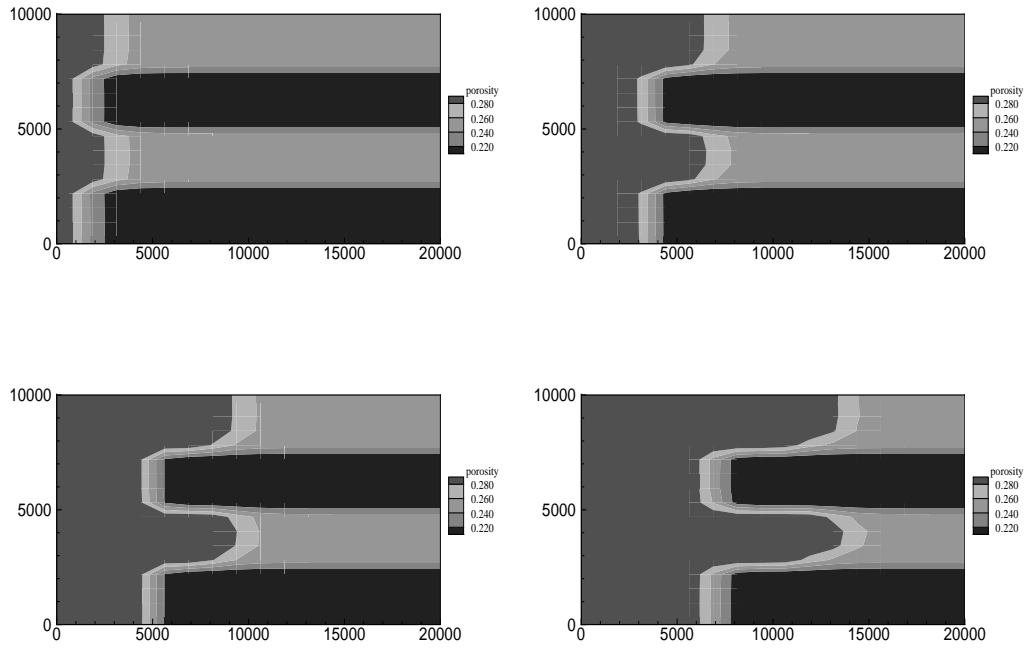
Figure 6.12: Solution contours for the porosity in Layered Porous Media with $V_f = 100$ cm/day with fewer layers

Figure 6.13: Solution contours for the concentration in Layered Porous Media with $V_f = 100$ cm/day with fewer layers
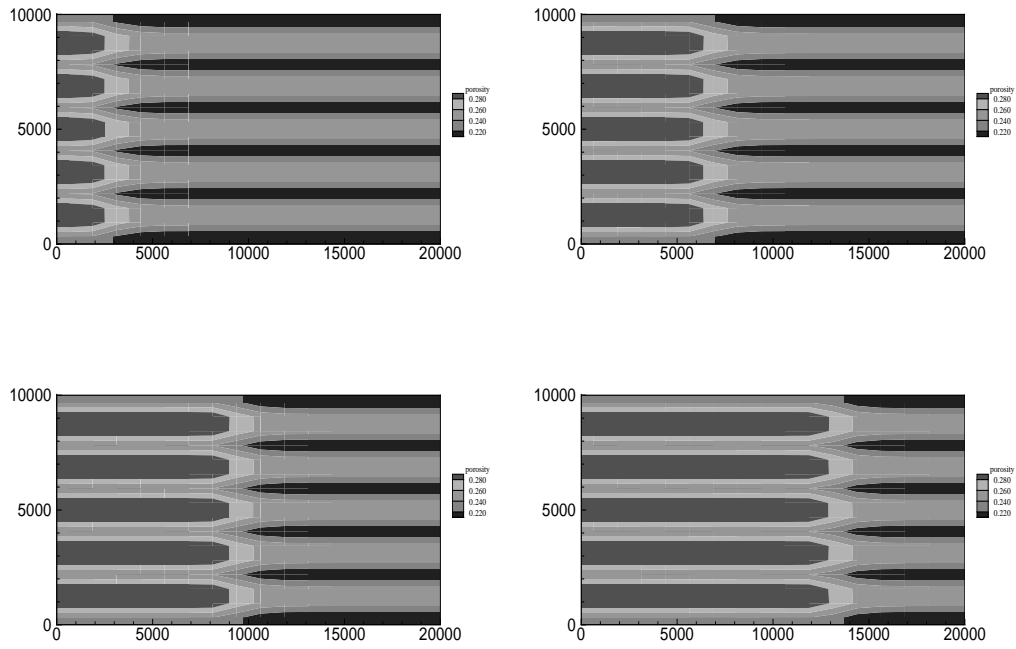
Figure 6.14: Solution contours for the porosity in Layered Porous Media with $V_f = 10$ cm/day with fewer layers

Figure 6.15: Solution contours for the concentration in Layered Porous Media with $V_f = 10$ cm/day with fewer layers

Figure 6.16: Solution contours for the porosity in Layered Porous Media with $V_f = 100$ cm/day

Figures 6.16–6.23 show the results for the second case. We note here that layering ahead and behind the front stabilizes the front.
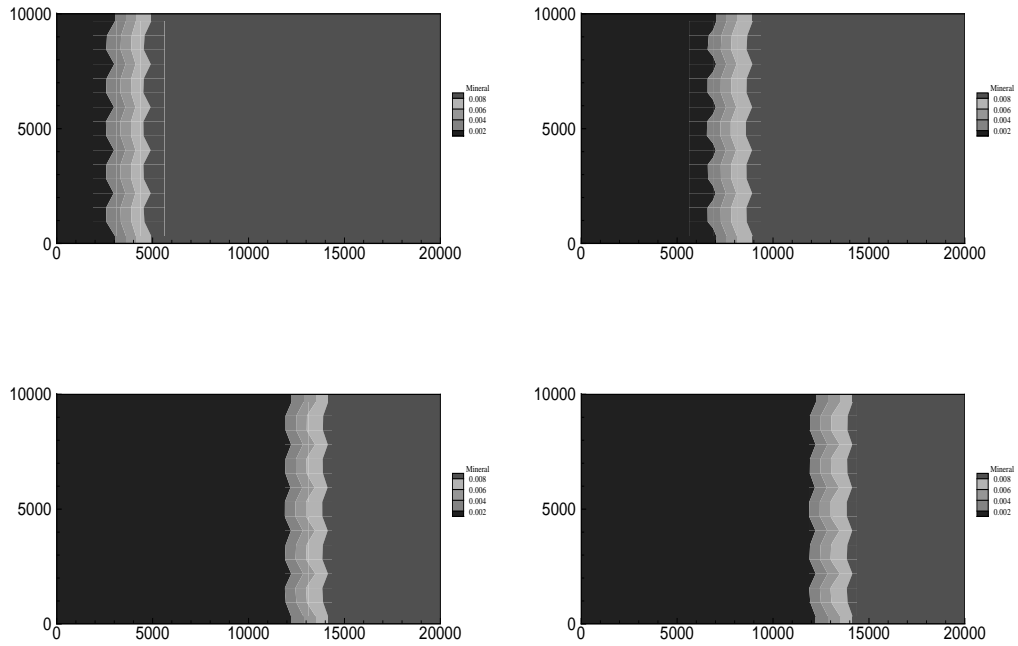
Figure 6.17: Solution contours for the concentration in Layered Porous Media with $V_f = 100$ cm/day
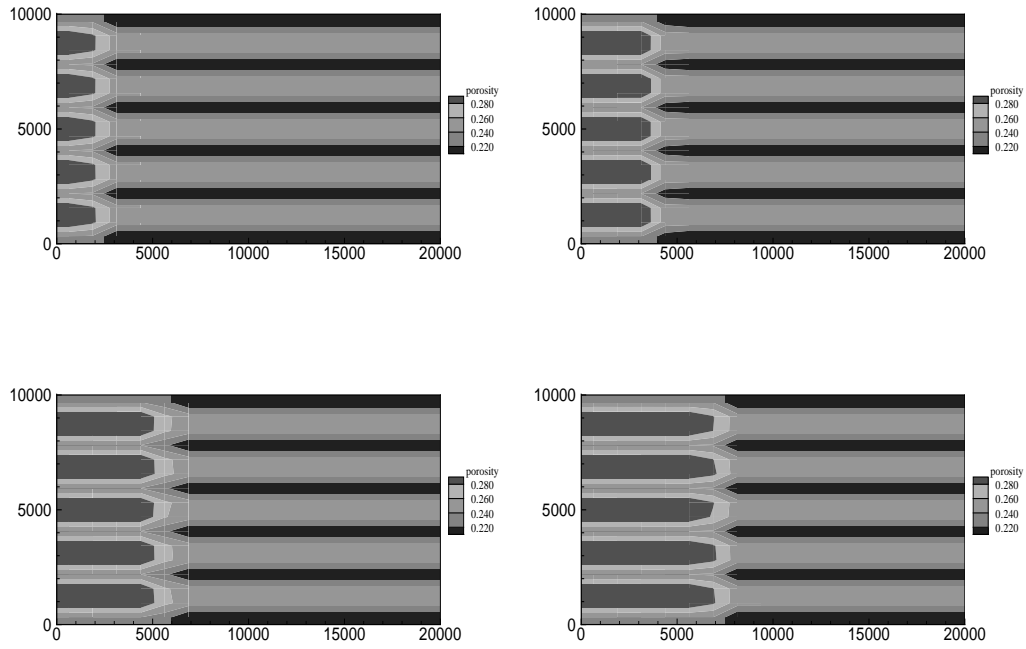
Figure 6.18: Solution contours for the porosity in Layered Porous Media with $V_f = 10$ cm/day
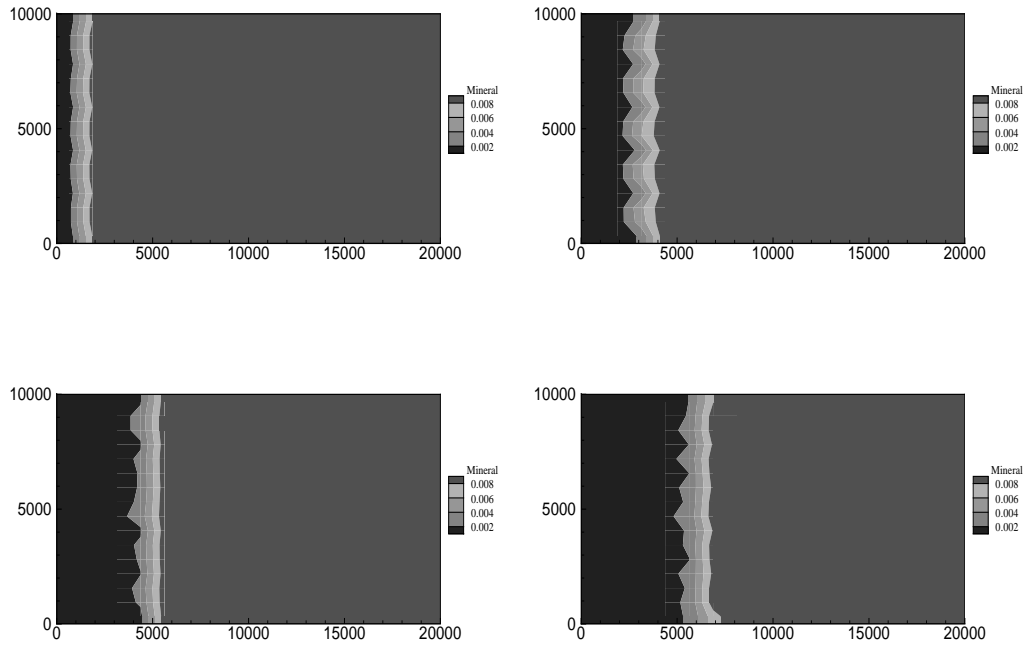
Figure 6.19: Solution contours for the concentration in Layered Porous Media with $V_f = 10$ cm/day
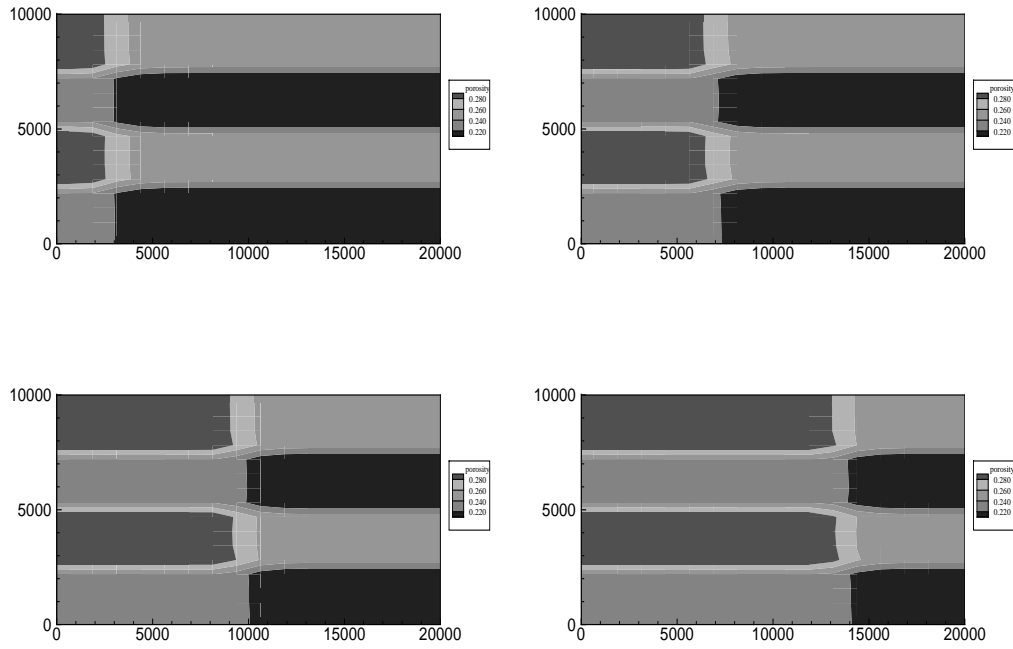
Figure 6.20: Solution contours for the porosity in Layered Porous Media with $V_f = 100$ cm/day and fewer layers
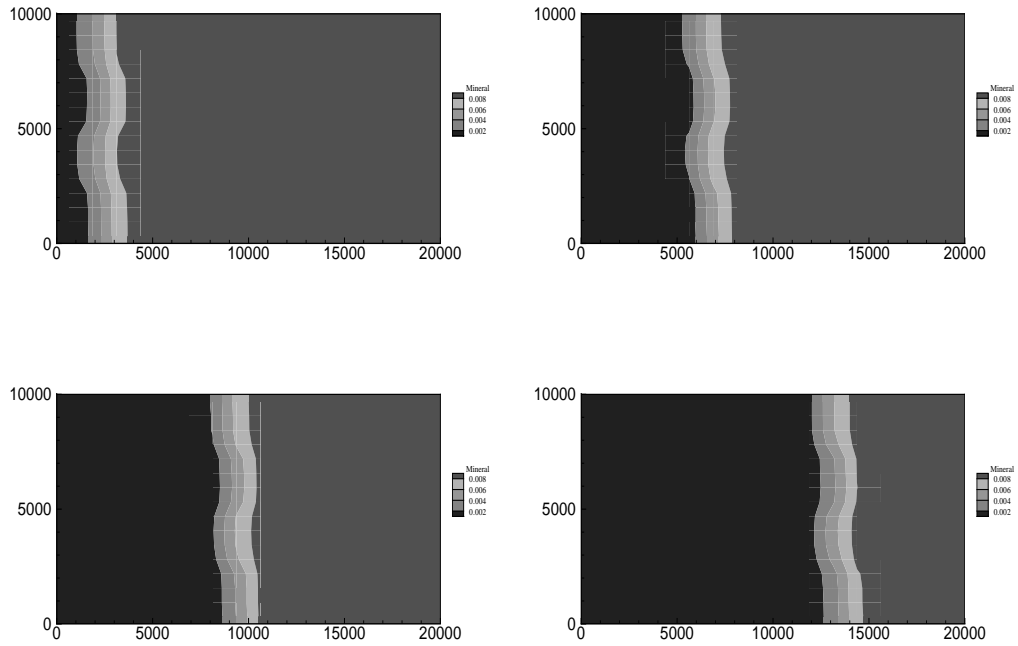
Figure 6.21: Solution contours for the concentration in Layered Porous Media with $V_f = 100$ cm/day and fewer layers
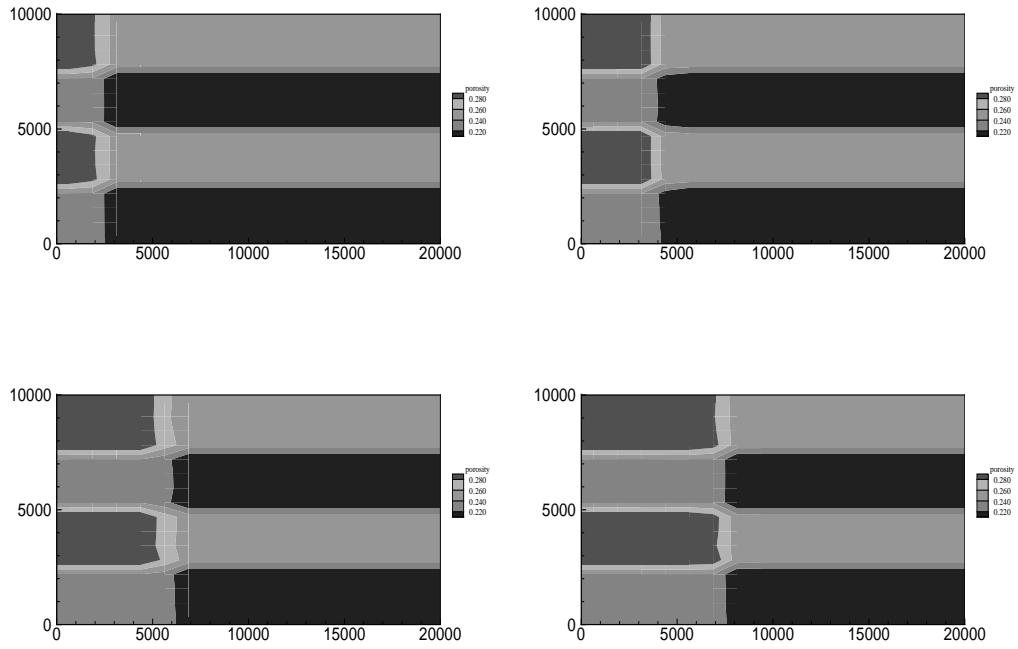
Figure 6.22: Solution contours for the porosity in Layered Porous Media with $V_f = 10$ cm/day and fewer layers
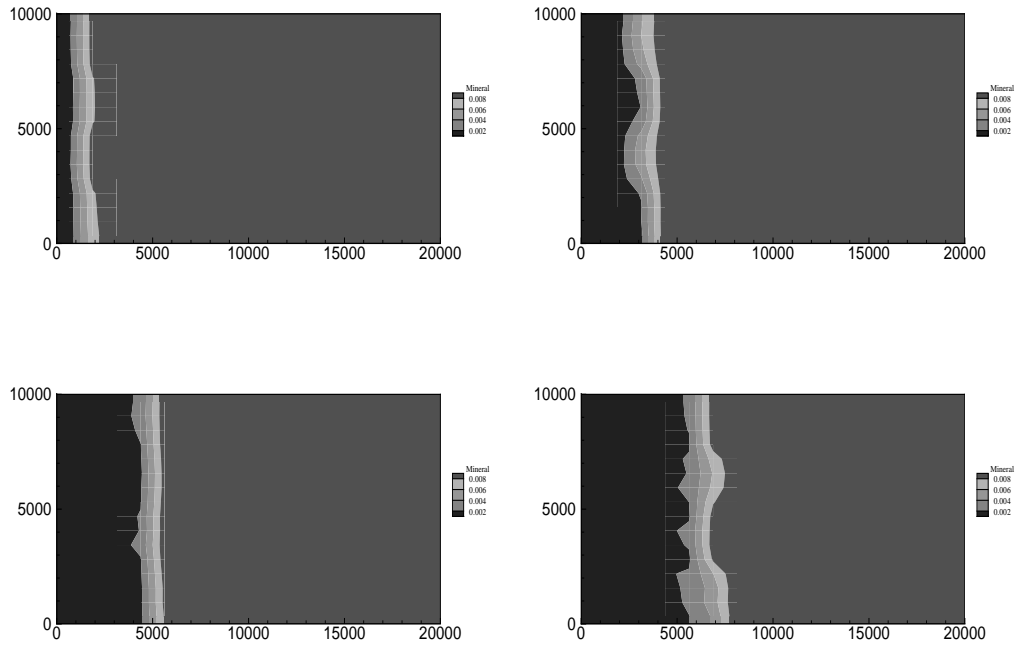
Figure 6.23: Solution contours for the concentration in Layered Porous Media with $V_f = 10$ cm/day and fewer layers
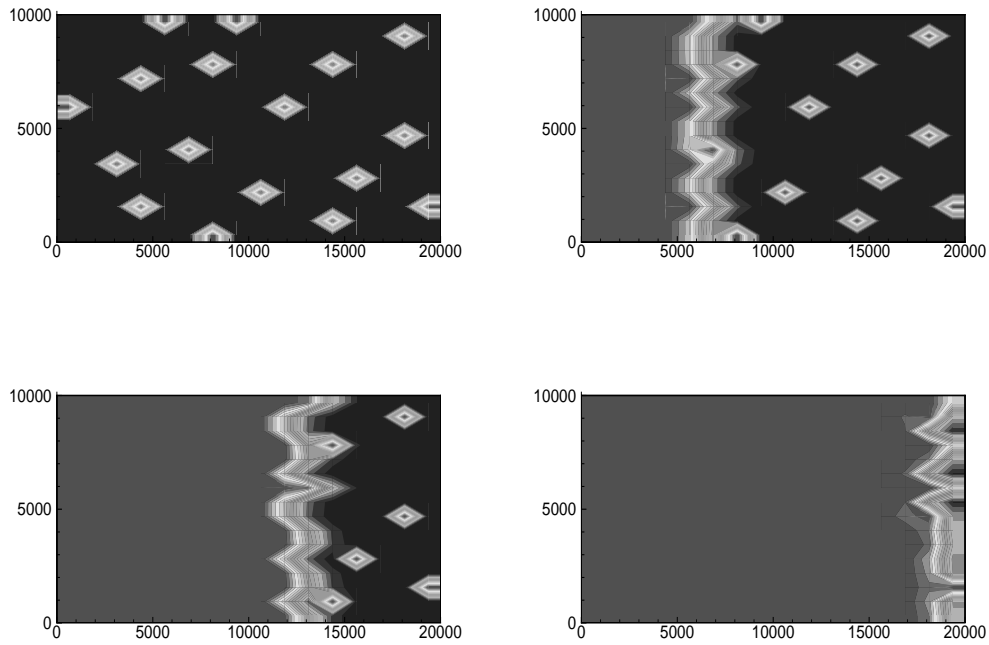
Figure 6.24: Solution contours for the porosity in a Heterogeneous Porous Media with $v_f = 100$ cm/day

6.7.2 Heterogeneous porous media

Medium heterogeneity is an important factor that affect the flow of multiphase fluid mixtures and the dispersion or dilution of aqueous chemical plumes in aquifers and petroleum reservoirs [36].

We first run the code for a case where the initial porosity is $\phi_0 = .25$ except at some random points where the porosity is equal to its final value 0.3. Figures 6.24 and 6.25 show the porosity contours. We notice that the shape of the front for the concentration is similar to porosity as shown in Figures 6.26 and 6.27.
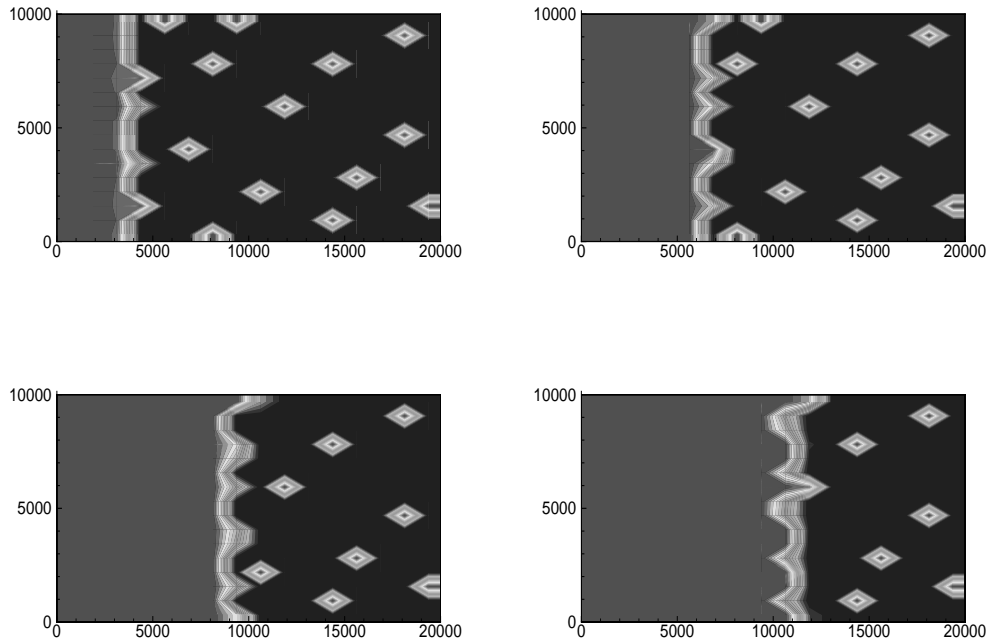
Figure 6.25: Solution contours for the porosity in a Heterogeneous Porous Media with $v_f = 10$ cm/day
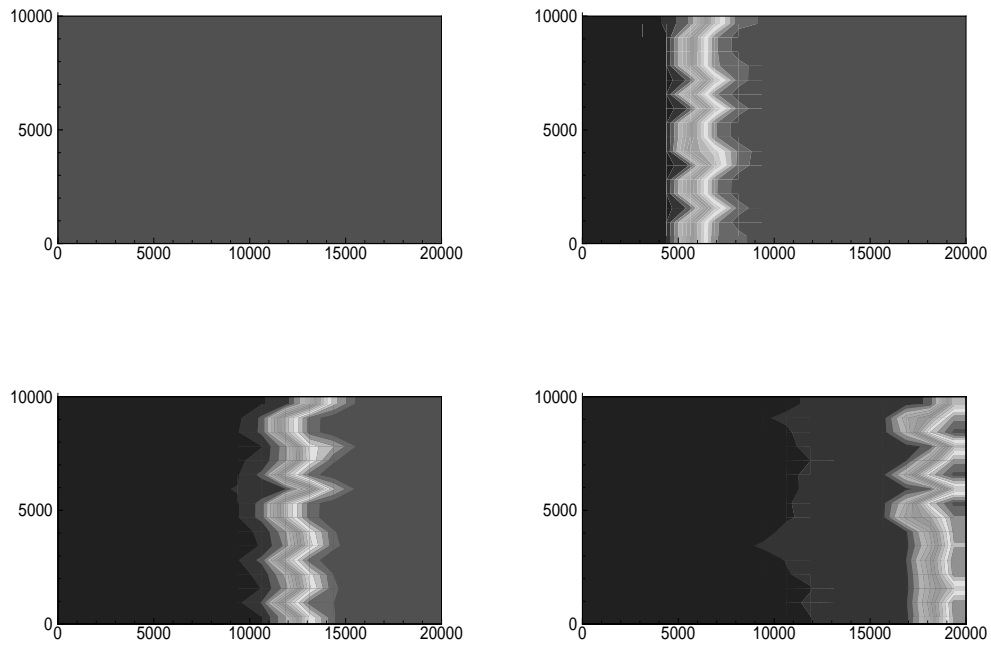
Figure 6.26: Solution contours for the concentration in a Heterogeneous Porous Media with $v_f = 100$ cm/day
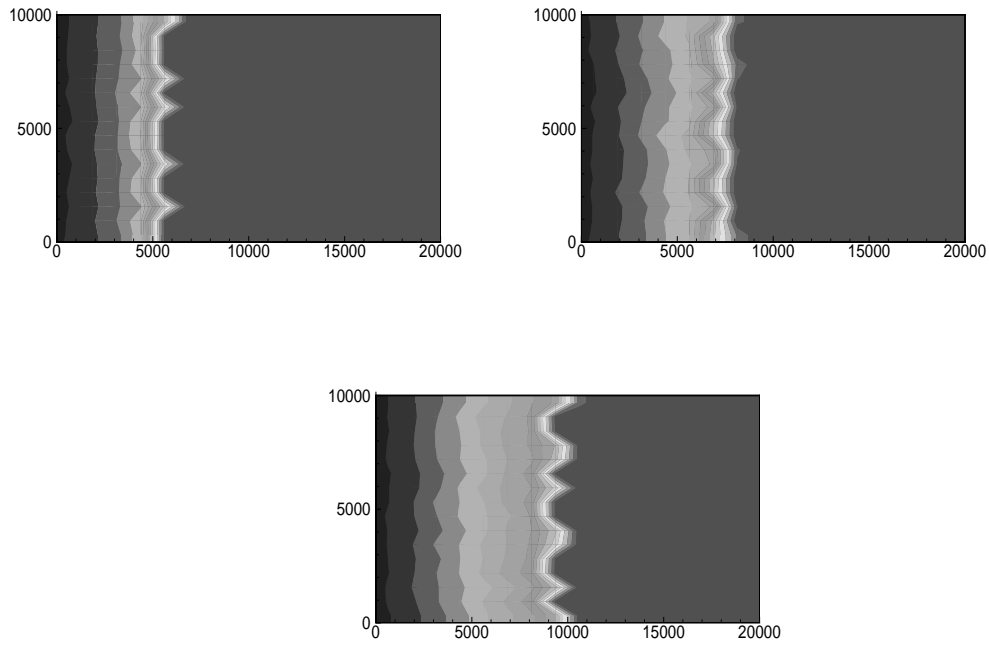
Figure 6.27: Solution contours for the concentration in a Heterogeneous Porous Media with $v_f = 10$ cm/day

Next, we run the code for a random porosity field. The initial heterogeneous porous medium is constructed by randomly assigning the porosity at each cell. The porosity has values between .1 and .5. The results are shown in Figure 6.28. Initially the concentration is assumed to be constant all over the domain with value equal to .01. The last graph of Figure 6.28 shows the fluid streamlines. We note in this case, as in the layered media case, that the concentration front has the same shape as the porosity front, as can be seen in Figure 6.29.
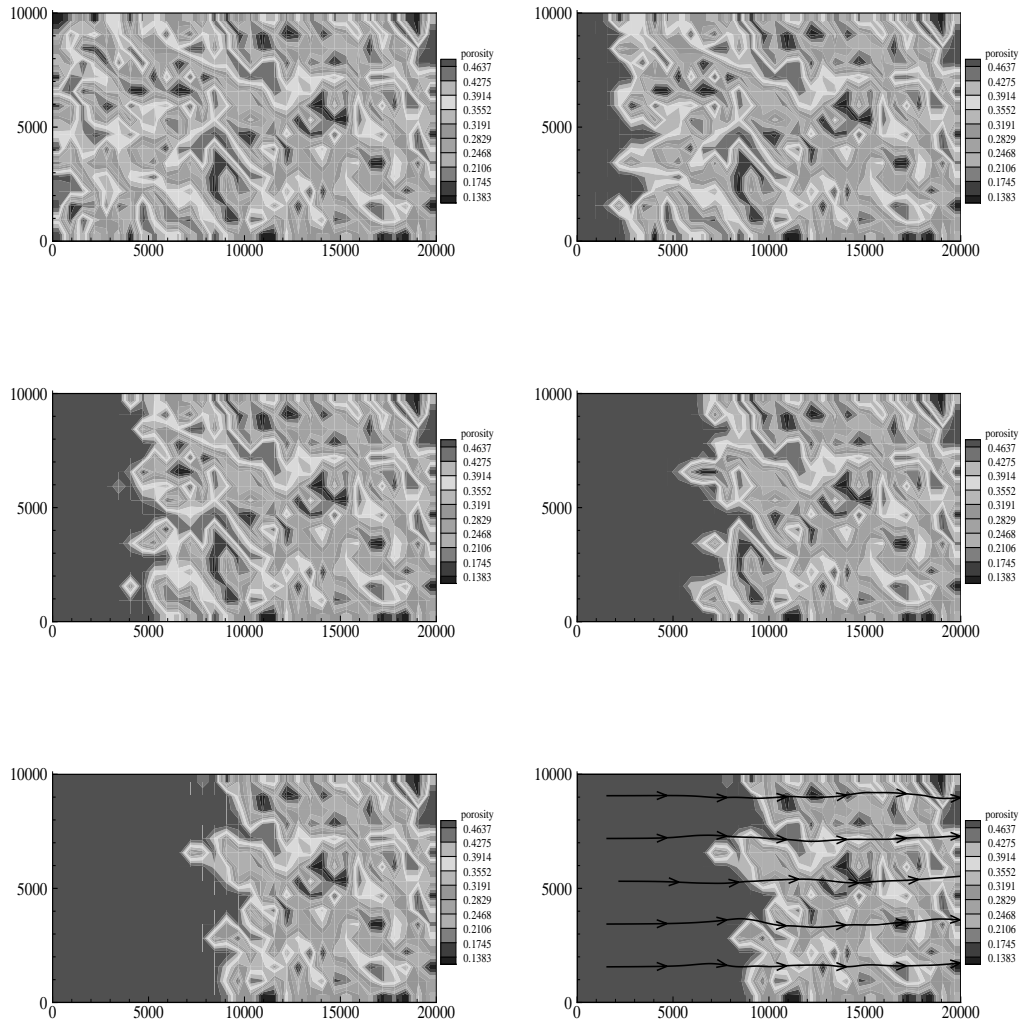
Figure 6.28: Solution contours for the porosity in a random Heterogeneous Porous Media with $v_f = 100$ cm/day
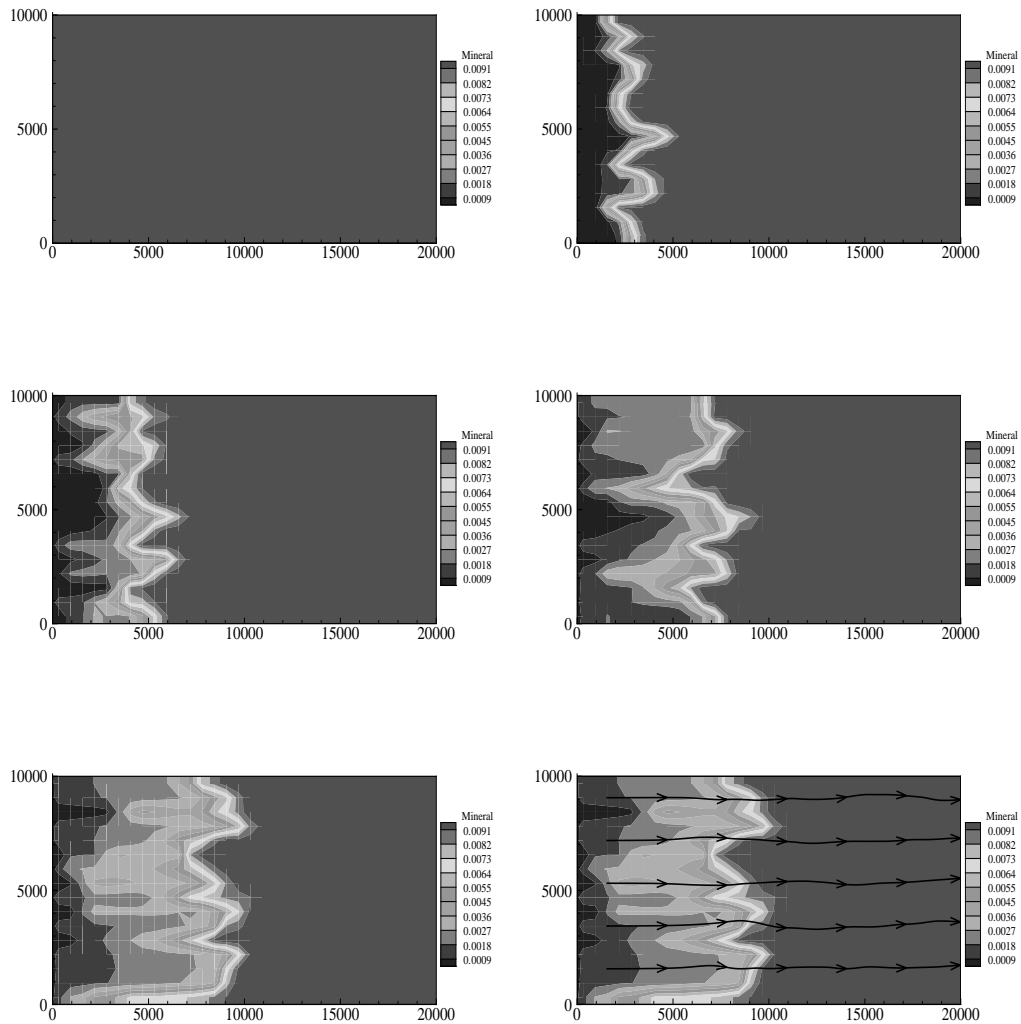
Figure 6.29: Solution contours for the concentration in a random Heterogeneous Porous Media with $v_f = 100$ cm/day

6.8   Real world problem

To apply the algorithm to a real world example, the problem explained by Zhu, Hu, and Burden in [39] and [40] is used. In these studies an abandoned uranium mill tailings site (the Bear Creek Uranium site) in Wyoming, USA was used to simulate natural attenuation of a contaminated aquifer. The aquifer is contaminated with sulfuric acid which was used to dissolve and oxidize uranium. The spent acids were piped to unlined tailings ponds. To reclaim the site, a low-permeability cover is to be installed on the tailings ponds to prevent further infiltration from precipitation. It is predicted that 5 years after the cover installation that tailings pore water will cease to drain into the underlying aquifer. After that time, the plume will be flushed by uncontaminated upgradient groundwater [39]. In their study, a total of 11 aqueous component, and six minerals were included in the simulations which was done using PHREEQC Version 2.0, a one-dimensional finite-difference model.

We will numerically simulate a period of 400 years of flushing of the contaminated aquifer by uncontaminated upgradient ground water and predict the concentrations of sulfate (SO_4^{2-}). This flushing will cause gypsum, $Ca(SO_4).2H_2O$, to dissolve out and this lead to an increase in porosity. For the sake of testing, we will only use a single component in the simulations. Table 6.4 summarizes the values used for different parameters and Figure 6.30 shows the domain used. In [40] the speed of

the gypsum-dissolution front was estimated using the following equation

$$\bar{v}\frac{C_2^a - C_1^a}{C_2^T - C_1^T},\tag{6.5}$$

where $\bar{v}$ is the pore velocity, C^a is concentration in the aqueous phase, and C^T is the total concentration of the component in both the aqueous and solid phases. The subscripts indicate the values upstream and downstream of the wavefront, respectively. They used Ca^{2+} concentration for calculation and came up with the value 2.83 m/yr. On that study, no porosity change was considered and local equilibrium was used in the above calculations.

Using equation (6.4) and the values given in Table 6.4, our model estimates the front velocity to be $V = 1.732$ m/yr, a close agreement.

Since the model used in [39] and [40] does not involve the reaction rate constant, k, we need to determine what value to use for this constant. Many geochemical studies were done to determine an accurate dissolution rates of gypsum (see for example [24] and [33]). According to these studies, there are many factors that control and affect the dissolution rates of gypsum including the chemical reaction at the surface, molecular diffusion, ionic strength, crystallographic orientation [24], [33]. From in-situ experiments done by the authors of [33], gypsum dissolution rates fell in the range of 0.1×10^{-5} (slow flow) to 2.0×10^{-5} $mol\ cm^{-2}\ h^{-1}$ (fast flow). We can note from equation (6.4) that the reaction rate constant, k, does not affect the speed of the front [12]. Therefore, in our simulation k is set to $10^3 yr^{-1}$. To represent the

v_f	50 m/yr	a_L	10 m
ϕ_0	0.2874 and 0.3	a_T	1 m
ϕ_f	0.3214	D	0
c_f	$8\ mol/m^3$	c_{eq}	$16\ mol/m^3$
ρ	$13434.396\ mol/m^3$		

Table 6.4: values used in real world problem

relationship between permeability and porosity, the P.C. Lichtner [28] equation given in Chapter 2 is used.

In Figure 6.31 the concentration contours are shown at 100 yr time interval, while Figure 6.32 shows the porosity contours. We note that the speed of the front in the numerical simulation is less than the theoretical value estimated above. From the graph the speed is found to be 1.625 m/yr.

To check for instability, we rerun the above case with an artificial bump, as done in the previous sections. The results are shown in Figure 6.33, and we note that the front is stable where the bump does not grow.

As predicted by the mathematical model of the Reaction-Infiltration instability problem, these numerical results showed that the porosity change cause the front to advance in a slower speed than the fluid flow. We note also that the front velocity is affected by the choice of the equation representing the relationship between
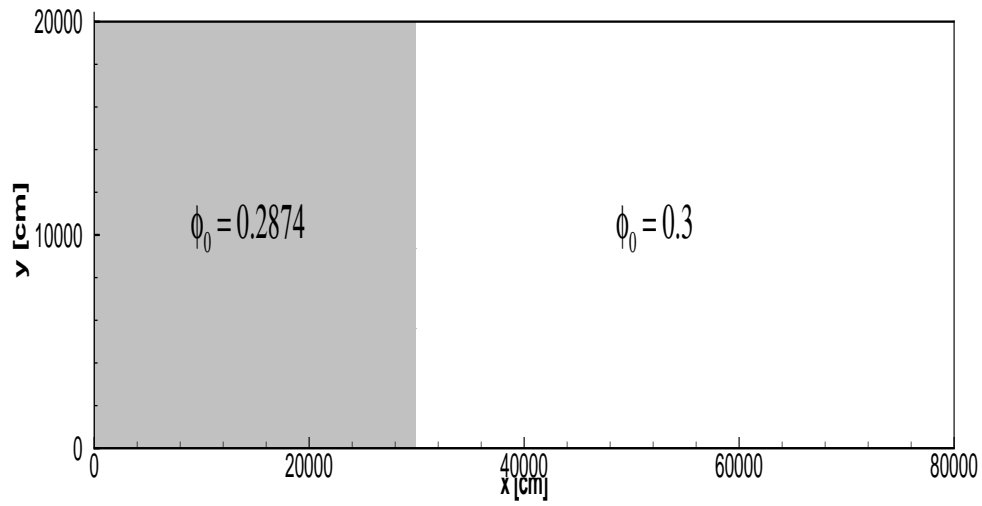
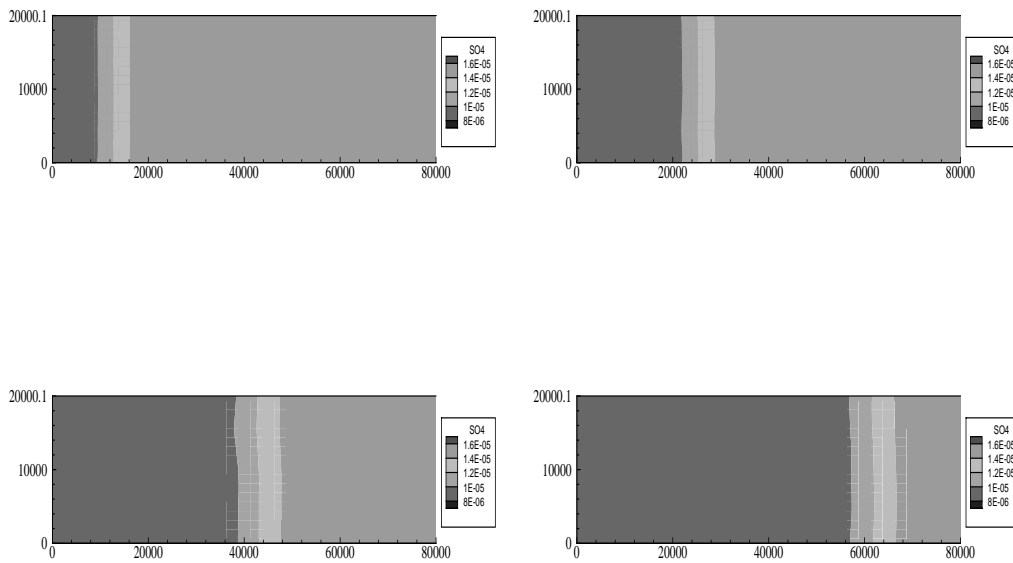Figure 6.30: Numerical Domain for real world problem

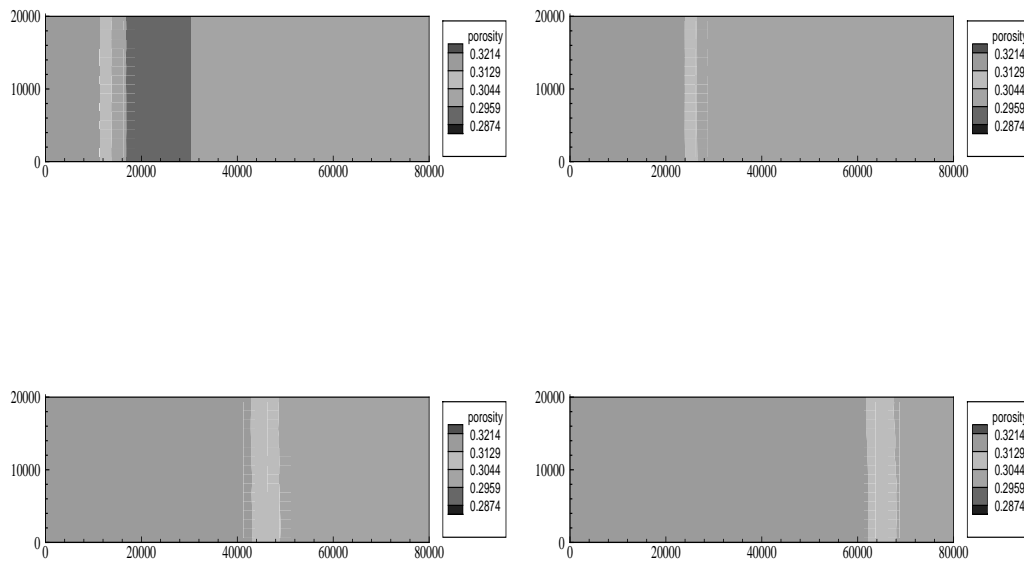Figure 6.31: Solution contours for the concentration

Figure 6.32: Solution contours for the porosity

porosity and permeability. Therefore, an accurate prediction of this relation may lead to a more realistic simulation of the real world problems.
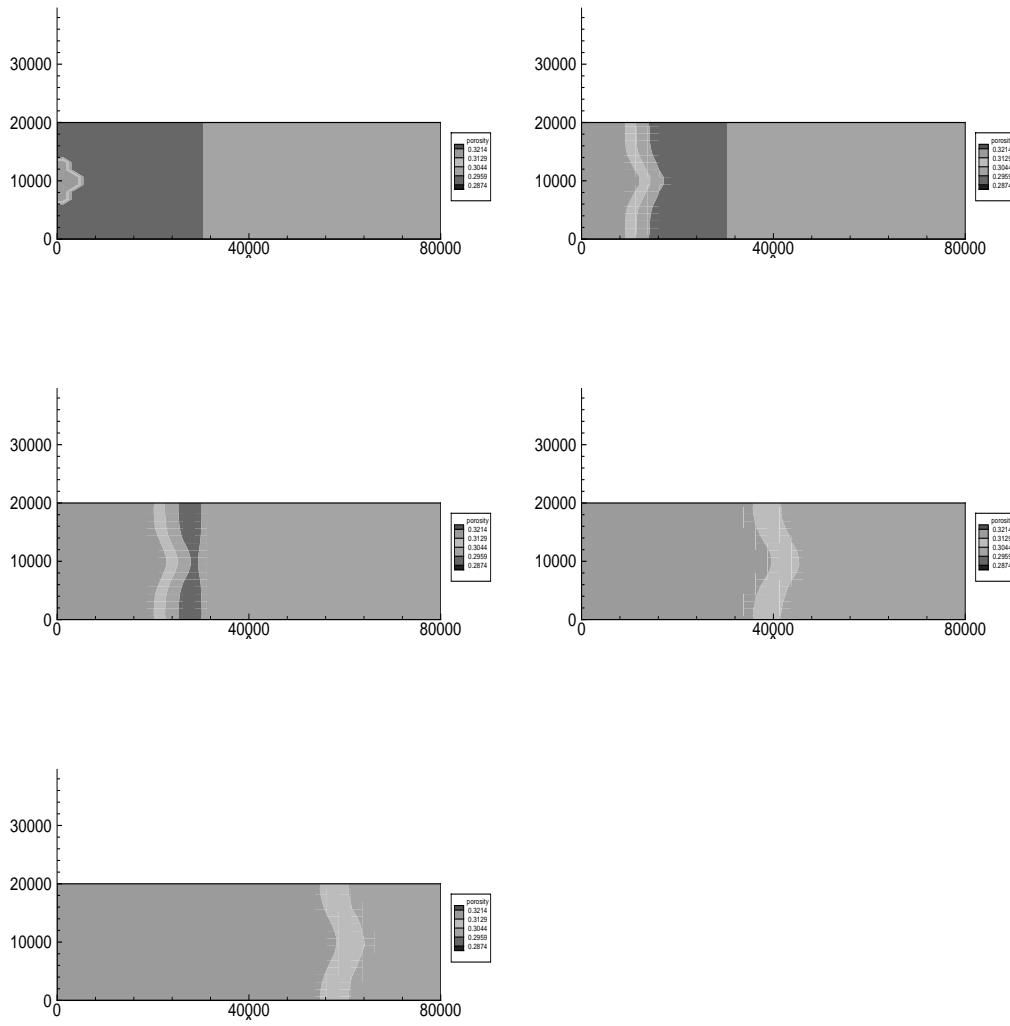
Figure 6.33: Porosity contours at $t = 0, 100, 200, 300, 400$ years